FLOW CAMBRIDGE
UNIVERSITY PRESS

RESEARCH ARTICLE

Dynamics of droplet formation in rotary flow focusing

Yihao Yang[1] , Jijie Fu[1], Kai Mu[1] , Shiyu Wang[2], Pingan Zhu[2] and Ting Si[1]

[1]Department of Modern Mechanics, University of Science and Technology of China, Hefei, PR China
[2]Department of Mechanical Engineering, City University of Hong Kong, Hong Kong, PR China
Corresponding author: Ting Si; Email: tsi@ustc.edu.cn

Abstract

Rotary flow focusing (RFF) is distinguished from conventional microfluidic platforms through its capacity to accommodate wide viscosity ranges in both continuous and dispersed phases during droplet formation. The dynamic mechanisms during droplet formation and the parametric dependencies within RFF systems are examined systematically. Four distinct flow modes, including squeezing, dripping, jetting and tip-streaming, are achieved by varying the rotational velocity and the dispersed-phase flow rate, and the corresponding transition boundaries are identified. In the squeezing and dripping modes, scaling laws are derived to predict droplet size based on interfacial dynamics during the breakup of the dispersed phase. In the jetting mode, functional relationships describing how jet diameter, droplet size and jet length depend on flow parameters are established through external flow field analysis. The tip-streaming mode facilitates the production of droplets at very small scale, with the effects of flow control parameters on droplet size quantitatively evaluated. Additionally, the effects of geometric parameters and fluid physical properties on RFF performance are investigated, enabling the successful production of high-viscosity fluid droplets ranging from micrometre to millimetre scales.

Impact Statement

In the field of microdroplet generation, the rotary flow focusing technique is distinguished from conventional emulsification, microfluidic and flow focusing methods by its simple structure, high throughput and broad material compatibility. In this technique, a narrow slit is formed by two cylindrical rotors, and a stable shear flow is induced within the narrow slit through their counter-rotation. The shear flow stretches the dispersed phase passing through a needle, leading to the formation of a jet or direct disintegration into droplets. The viscous forces of the continuous phase are exploited to enhance interfacial shear, rendering the technique particularly suitable for the generation of microdroplets from high-viscosity fluids. Furthermore, due to the externally applied rotary flow field, no supply of additional continuous phase is required during the droplet generation process. In this study, theoretical guidance is provided for the efficient generation of high-viscosity microdroplets, with great potential applications identified in biomedicine, energy, environmental technologies and advanced materials.

1. Introduction

Microdroplets involve many kinds of materials and have extensive applications, demonstrating significant value in fields such as biomedicine, advanced materials and environmental energy. For example, in the field of biomedicine, microdroplets can be employed as discrete reaction vessels with independently tunable conditions, enabling reduced reagent consumption and minimising cross-contamination

(Li *et al.* 2022; Xu *et al.* 2020). Such features are particularly valuable in applications such as small-molecule detection, protein analysis and drug screening. In the development of advanced functional materials and engineering applications, liquid metal microdroplets are extensively used in processes such as inkjet printing (Li *et al.* 2018) and the fabrication of conductive composites (Markvicka *et al.* 2018; Yun *et al.* 2019). The generation of these microdroplets typically requires complex processing conditions, including the application of strong shear forces and the handling of high-viscosity materials. Specific applications often impose stringent requirements regarding droplet size, yield, uniformity and surface morphology. Consequently, the preparation of microdroplets encounters numerous challenges.

Conventional microdroplet generation methods primarily include emulsification and microchannel techniques. The emulsification method alters the interfacial properties of emulsions through physical or chemical approaches, such as mechanical stirring (Hert *et al.* 2018; Liang *et al.* 2022), ultrasonic treatment (Hohman *et al.* 2011) or the addition of emulsifiers, resulting in the fragmentation of the dispersed phase into numerous small droplets within an immiscible continuous phase (Saffarionpour 2019; Sheth *et al.* 2020). This method is user-friendly and capable of producing a large quantity of droplets simultaneously. However, the non-uniform external force field during this process often results in droplet polydispersity, as well as other limitations, including high energy consumption, broad size distribution and poor reproducibility. Microchannel methods, including microfluidic chips (Garstecki *et al.* 2005; Zhu & Wang 2017; Cubaud & Mason 2008; He *et al.* 2025) and glass microcapillaries (Utada *et al.* 2005, 2007; Marín *et al.* 2009; Guerrero *et al.* 2020), stabilise flow at the microscale by exploiting surface tension and viscous effects, resulting in droplets with high uniformity. However, the closed structure of these devices limits fluid flux and shear strength within the microchannel, leading to low productivity, restricted material compatibility and challenges in integration, which significantly hinder the practical applications of microfluidic technology.

The flow focusing (FF) technique (Gañán-Calvo 1998, 2007) is an emerging method, in which a high-speed outer fluid compresses and accelerates an inner fluid, forming a jet that subsequently breaks up into microdroplets in an open space (Zhu *et al.* 2023). Subsequent studies (Rosell-Llompart & Gañán-Calvo 2008; Herrada *et al.* 2008) provided theoretical predictions for jet diameter, incorporating the effects of fluid viscosity and interfacial tension. The influence of primary control parameters on droplet formation has been systematically investigated, thereby promoting the advancement of FF technology (Mu *et al.* 2019; Si *et al.* 2009; Si 2021). Experimental findings (Gañán-Calvo & Barrero 1999) have demonstrated that the variations in liquid flow rate and continuous gas pressure drop give rise to multiple flow modes. Moreover, dimensional analysis and linear stability theory have been utilised to predict the transition boundaries between these modes (Gañán-Calvo & Montanero 2009; Si *et al.* 2010; Vega *et al.* 2010). Although FF enables the generation of monodisperse microdroplets, its application to highly viscous fluids and system integration remains constrained. As geometric dimensions decrease, viscous effects become dominant, leading to heightened sensitivity of device performance to flow parameters and diminished efficacy in high-viscosity applications.

Due to the inefficiency of existing methods in generating high-viscosity microdroplets, the rotary flow focusing (RFF) technique has been developed recently. The principle of RFF can be described as the rotation of a symmetric rotor inducing strong shear forces at a slit, leading to the fragmentation of the dispersed phase exiting a needle into microdroplets. For instance, some researchers have explored flow characteristics in double-rotor configurations (Dormy & Moffatt 2024; Jeffery 1922), while Taylor examined how a four-rotor flow field influenced droplet breakup at the flow centre (Taylor 1934). In our recent studies, liquid metal droplets with characteristic conical tails have been rapidly produced by RFF, exhibiting electrostatic responsive behaviour and showing potential for applications in micromotor design and soft electronics (Wang *et al.* 2021). Nevertheless, research on RFF remains limited, with parameter selection and operating conditions largely determined by empirical methods in comparison with FF techniques. Comprehensive investigations into interfacial dynamics during droplet formation are still lacking, and the effects of key control parameters on droplet size, yield and uniformity have not yet been clarified.
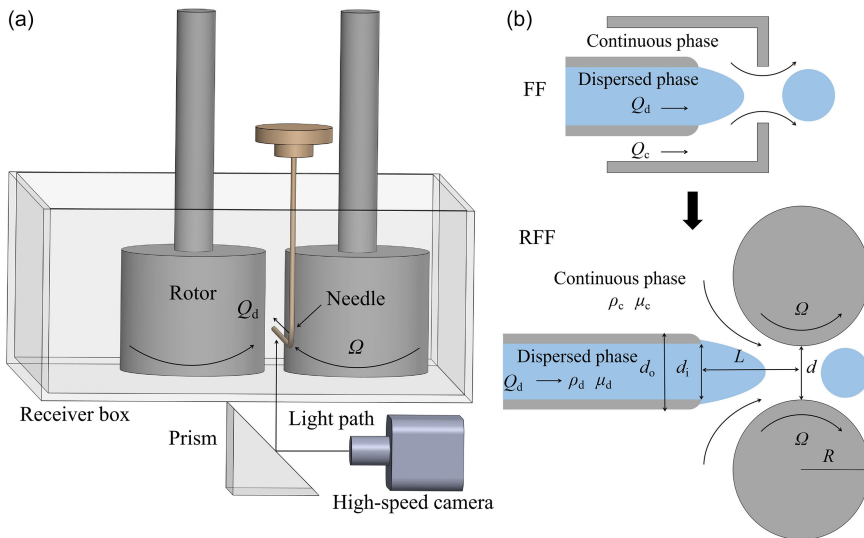
Figure 1. *(a) Three-dimensional schematic of the RFF device. (b) Mechanistic comparison between FF and RFF.*

In this study, the interfacial flow dynamics in RFF is systematically investigated through the integration of experimental observations and numerical simulations. Initially, the experimental method is briefly introduced. Subsequently, typical interfacial evolution modes are classified, and quantitative relationships between droplet size and governing parameters are derived for each flow mode. Theoretical and computational analyses are performed to interpret the experimental findings. In addition, the effects of key geometric parameters and fluid physical properties on droplet formation are evaluated. Microdroplets ranging from micrometres to millimetres in size are successfully produced using highly viscous fluids. Finally, the principal conclusions of the study are presented.

2. Experimental methods

A schematic diagram of the RFF device is presented in figure 1(*a*). Under motor control, the rotors are driven to rotate in opposite directions at identical speeds via a gear-based transmission system, generating a stable shear flow in the continuous phase between them. This shear is primarily induced by the rotation of the rotor sidewalls. The outlet needle is fixed at the entrance of the rotor gap using a 3D-printed bracket, positioned at the lower centre to minimise three-dimensional effects from the top and bottom ends of the rotors. As the dispersed phase flows throughout the needle, it is subjected to shear from the continuous phase and subsequently breaks into microdroplets. The process is governed by two primary external flow parameters: the dispersed-phase flow rate Q_d and the rotational velocity ΩR. Flow rate Q_d is precisely regulated via a syringe pump (resolution: $0.1 \, \mu l \, min^{-1}$), while Ω is controlled through PWM-driven motor actuation. Due to obstruction of the rotors and the needle holder, direct observation of the fluid dynamics in the rotor gap from the horizontal plane is not feasible. To enable side-view imaging of the flow field, a right-angled prism is placed beneath the fluid collecting container, as shown in figure 1(*a*).

While RFF exhibits distinct geometric configurations compared with FF, both systems share similar fundamental operating principles. As illustrated in figure 1(*b*), both configurations induce high-speed continuous phase in the vicinity of needle exit to shear the dispersed phase. The primary distinction lies in the mechanism by which the continuous phase is actuated: FF utilises pressure differentials to induce flow, while RFF employs rotor rotation to drive the continuous phase. This rotational mechanism transforms the role of the channel boundaries from passive flow resistors into active flow enhancers,

allowing high-viscosity continuous-phase fluids to generate stronger interfacial shear forces. In addition, the simple structure of RFF facilitates system integration. By extending the rotor length and arranging multiple needles vertically in parallel, scalable multichannel production can be achieved. Overall, compared with FF, RFF offers stronger interfacial shear forces and greater ease of integration, presenting distinct advantages in the massive generation of high-viscosity microdroplets.

In the experiment, the geometric parameters in RFF are given as follows: needle-to-rotor-connection-midpoint distance L, rotor spacing d, rotor radius R and needle diameters d_i (inner) and d_o (outer). For the experimental set-up, the geometric parameters are $d_i = 157\,\mu m$, $d_o = 362\,\mu m$ and $R = 6.92\,mm$; L and d are adjustable. Unless otherwise specified, $L = 2\,mm$ and $d = 0.3\,mm$. In the main content of this study, 90 wt% glycerol aqueous solution is selected as the continuous phase. The dynamic viscosity and density of the glycerol aqueous solution are $\mu_c = 171.5\,mPa\,s$ and $\rho_c = 1.253\,g\,ml^{-1}$, respectively. The dispersed phase consists of silicone oil, which is dyed with an appropriate amount of blue-oil-based dye to facilitate the observation of experimental phenomena. The dynamic viscosity and density of the dispersed phase are $\mu_d = 9.15\,mPa\,s$ and $\rho_d = 0.933\,g\,ml^{-1}$, and the interfacial tension $\gamma = 29.75\,mN\,m^{-1}$. The corresponding dimensionless parameters are as follows: Reynolds number of the dispersed phase $Re_d = \rho_d u_d d_i / \mu_d$ (with the dispersed-phase characteristic flow velocity $u_d = 4Q_d/(\pi d_i^2)$), capillary number of the continuous phase $Ca_c = \mu_c u_c / \gamma$ (with the continuous-phase characteristic flow velocity $u_c = \Omega R$), density ratio $S = \rho_d/\rho_c$ and viscosity ratio $N = \mu_d/\mu_c$. For comparison, a series of glycerol aqueous solutions with different viscosities and silicone oil are also used in subsequent experiments. To ensure the reliability of the phase diagrams, more than three experimental repetitions are performed under identical conditions near the mode transition boundaries. For the measurement of characteristic quantities such as droplet diameter, at least 10 data points are averaged. The associated error bars and relevant parameters have been clearly indicated in corresponding figures and captions.

3. Results and discussion

3.1. Flow modes and phase diagram

By varying the dispersed-phase flow rate (e.g. $0.5 \leq Q_d \leq 90\,\mu l\,min^{-1}$) and the rotational velocity (e.g. $0.003 \leq \Omega R \leq 0.482\,m\,s^{-1}$), four fundamental modes of droplet generation are observed in RFF: squeezing, dripping, jetting and tip-streaming modes. Representative images of each mode are shown in figure 2(a). In the squeezing and dripping modes, the dispersed phase undergoes periodic stretching and breakup at the needle tip, forming highly uniform microdroplets within the slit. Mechanically, these two modes are fundamentally similar, both resulting from the interaction between the shear forces of the two-phase fluid and interfacial tension, which leads to droplet formation. However, the morphological characteristics differ between them. In the squeezing mode, the dispersed phase entirely fills the rotor gap before breakup, producing droplets much larger than the rotor spacing. In contrast, in the dripping mode, the dispersed phase does not contact the rotor wall upon droplet formation, resulting in smaller droplets. Unlike FF or microchannels with fixed walls, the RFF in squeezing mode, characterised by a lower rotational velocity, restricts the dispersed phase from moving against the rotor wall during the initial droplet formation stage. As the dispersed phase fills the front of the gap, the rotor wall's stretching action enables it to traverse the gap and form droplets. This dynamic rotor wall mechanism allows the RFF technique to efficiently generate larger droplets. In the jetting mode, the dispersed phase is ejected from the needle, forming a jet that breaks into droplets at its tip due to capillary instability. Unlike conventional jet flows, the slit shape constraints result in a longer conical structure in front of the needle, with the jet exhibiting a larger diameter at both ends and a narrower centre. The formation mechanism of this unique jet structure will be further analysed based on numerical simulations of the external flow field. In the tip-streaming mode, a stable cone of dispersed fluid forms at the needle tip, from which a microjet emerges and subsequently breaks into small droplets. These droplets are typically one to two orders of magnitude smaller than the needle diameter. Through these four flow modes, RFF demonstrates the ability to produce droplets spanning at least three orders of magnitude in size (micrometre to millimetre), combining the advantages of FF while exhibiting novel characteristics of droplet formation.
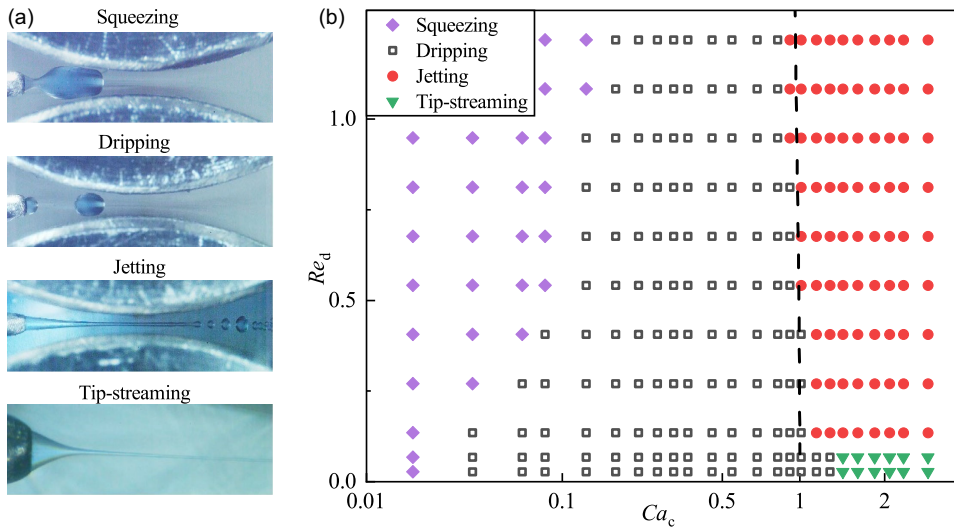
Figure 2. *(a) Representative images of RFF in various flow modes. (b) Dimensionless phase diagram of RFF, with the transverse axis Ca_c representing rotational velocity (ΩR) and the longitudinal axis Re_d representing the dispersed-phase flow rate (Q_d). The dashed line represents $Ca_c + We_d = 1$. (Geometric parameters: $L = 2$ mm and $d = 0.3$ mm.)*

The dimensionless phase diagram for RFF is presented in figure 2(*b*). As Ca_c increases, the interfacial shear force also increases, leading to a transition from squeezing to dripping, and ultimately to jetting mode. For microchannel flow, jetting mode occurs when the sum of the viscous forces exerted by the continuous fluid and the dispersed fluid inertia overcomes the interfacial tension forces, which is expressed as $Ca_c + We_d \geq 1$ (Utada *et al.* 2007), as indicated by the dashed line in figure 2(*b*). Given that the experimental parameters yield $We_d = \rho_d u_d^2 d_i/\gamma \sim 10^{-2}$, the dashed line can be approximated as $Ca_c \approx 1$. This result suggests that, under the experimental conditions, the dripping-to-jetting transition in RFF follows a similar criterion to that of microchannel flow. At low capillary numbers (e.g. $Ca_c < 1$), the surface tension dominates and maintains the dispersed phase in the dripping mode; whereas at $Ca_c > 1$, the interfacial shear stress of the continuous phase exceeds the interfacial tension, initiating the transition to the jetting mode. In the tip-streaming mode, the transition from a conical tip to a fine jet requires that the interfacial shear force overcomes the constraint imposed by the interfacial tension at the characteristic scale of the jet diameter. Under such high-speed external flow conditions, the shear force is predominantly governed by the viscosity of the continuous phase, indicating that the capillary number of the continuous phase should satisfy $Ca_c \geq 1$. Additionally, the Reynolds number of the dispersed phase should remain sufficiently low (e.g. $Re_d \ll 1$) to ensure that the viscous forces dominate, allowing the momentum transferred at the interface to be effectively diffused within the dispersed phase (Marín *et al.* 2009).

3.2. Quantitative analysis of squeezing and dripping modes

In the squeezing and dripping modes, the droplet size is comparable to the needle diameter, typically of the order of hundreds of micrometres. Figure 3(*a*) presents droplets generated under specific parameters, which exhibit good uniformity. During the experiment, droplets collected under different parameters are measured. Figure 3(*b*) shows the influence of flow control parameters – rotational velocity (ΩR) and dispersed-phase flow rate (Q_d) – on the dimensionless droplet size (D_d/d_s). These parameters correspond to the dimensionless numbers Ca_c and Re_d, respectively. The variable d_s represents the diameter of the contact line between the interface and the needle, as depicted in figure 3(*c*). When Re_d is held
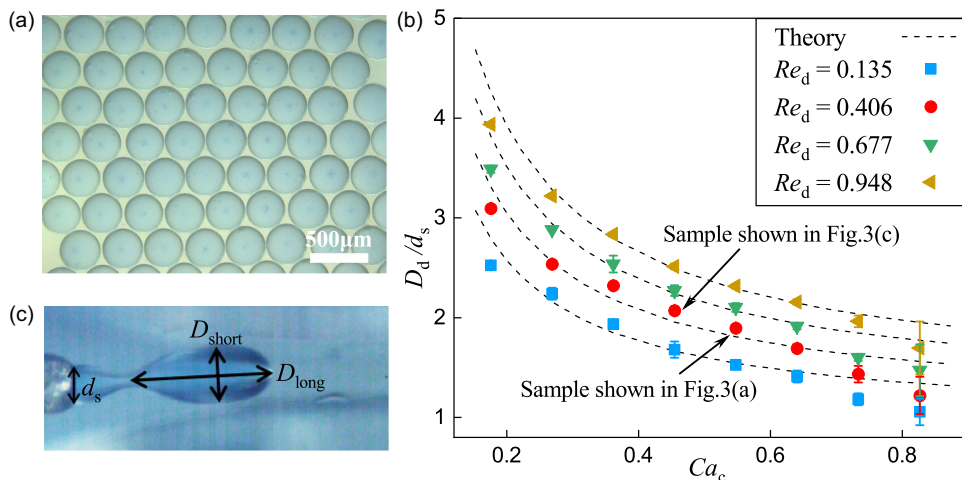
Figure 3. *Squeezing and dripping modes in RFF (geometric parameters: $L = 2$ mm and $d = 0.3$ mm). (a) Images of resulting droplets, with a scale bar of $500\,\mu$m ($Ca_c = 0.548$, $Re_d = 0.406$). (b) Dimensionless droplet size, calculated from experiments and theoretical predictions, as a function of Ca_c. The dashed lines represent the results of (3.3). (c) Morphology of the dispersed-phase interface when the droplet is about to break ($Ca_c = 0.455$, $Re_d = 0.406$).*

constant, an increase in Ca_c, which enhances the shear force between the interfaces, results in a reduction of droplet size. Additionally, a decrease in Re_d, representing a reduction in the dispersed-phase flow rate, also leads to smaller droplets.

To quantitatively explore the relationship between droplet diameter and experimental parameters, the detachment of the droplets at the needle tip is analysed. Figure 3(*c*) shows that droplets can be approximated as ellipsoidal during separation. The two minor axes of the ellipsoid are approximately equal and are denoted as D_{short}, while the long axis is denoted as D_{long}. The ratio of the long axis to the minor axis is defined as $K = D_{long}/D_{short}$, a value primarily determined by Re_d.

During droplet detachment, the force preventing droplets from detaching from the needle tip is the interfacial tension, given by $F_\gamma = \pi\gamma d_s$. In contrast, the forces promoting droplet generation include the momentum transfer force $F_I = 4\rho_d Q_d^2/(\pi d_s^2)$ and the viscous force $F_\mu = 3\pi\mu_c(u_c - u_{droplet})(D_{short} - d_s)$. The viscous force is derived from a modified Stokes formula, in which the characteristic length is defined as $(D_{short} - d_s)$. Here, D_{short} represents the droplet diameter in the flow direction, while d_s accounts for the influence of the needle on the force acting upon the droplet (Umbanhowar *et al.* 1999). In the equation for viscous force, the droplet velocity $u_{droplet} = 4Q_d/(\pi D_{short}^2)$ and the continuous-phase velocity is $u_c = \Omega R$. Additionally, the droplets are subjected to buoyancy in the vertical direction, given by $F_g = \pi K D_{short}^3 g(\rho_c - \rho_d)/6$. Since the buoyancy and momentum transfer forces are three orders of magnitude smaller than the viscous forces and surface tension within the experimental parameter range, they are considered negligible. By balancing the viscous force and interfacial tension, the following equation is obtained:

$$\pi\gamma d_s = 3\pi\mu_c(u_c - u_{droplet})(D_{short} - d_s). \tag{3.1}$$

After simplification and non-dimensionalisation, the following equation is derived:

$$\bar{d}^3 - \left(1 + \frac{1}{3Ca_c}\right)\bar{d}^2 - \varphi\bar{d} + \varphi = 0, \tag{3.2}$$

where $\bar{d} = D_{short}/d_s$ and $\varphi = 4Q_d/(\pi\Omega R d_s^2)$. Elliptical droplets become spherical under the influence of surface tension after passing through the narrow slit. Let the diameter of the spherical droplet be D_d. Using the volume conservation principle, the volumes of spherical droplet and the elliptical droplet can
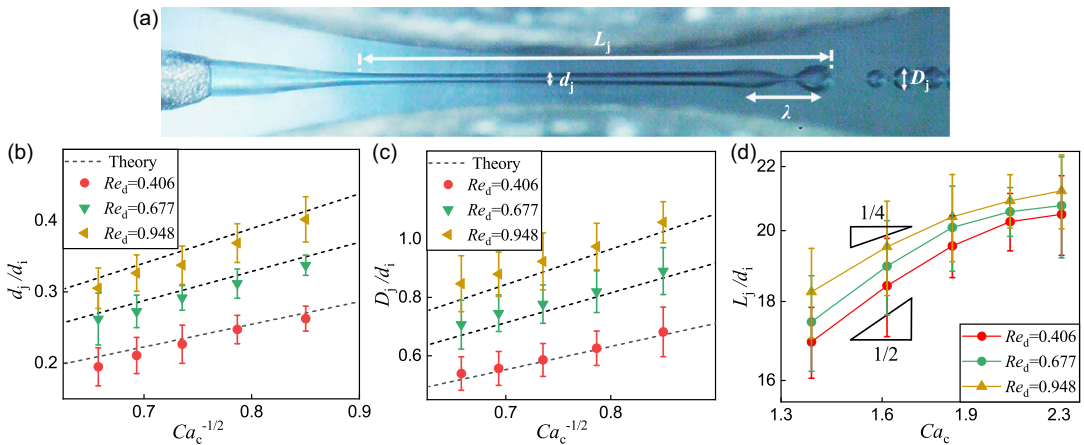
Figure 4. *Jetting mode in RFF (geometric parameters: $L = 2$ mm and $d = 0.3$ mm). (a) Typical images ($Ca_c = 1.38$, $Re_d = 0.406$). (b) Dimensionless jet diameter d_j/d_i, calculated from experiments and theoretical derivations, as a function of Ca_c under varying Re_d values. (c) Dimensionless droplet diameter D_j/d_i, calculated from experiments and theoretical derivations, as a function of Ca_c under varying Re_d values. (d) Dimensionless jet length L_j/d_i as a function of Ca_c under varying Re_d values.*

be give as: $\frac{4}{3}\pi D_d^3 = \frac{4}{3}\pi K D_{short}^3$. This yields the following relation:

$$D_d = AK^{1/3}\bar{d}d_s, \tag{3.3}$$

where A is a fitting constant, with a value of $A = 0.81$, and $d_s = 181$ μm in the experiment. The value of K under different Re_d values is given as follows: $K \approx 1.61$ when $Re_d = 0.135$, $K \approx 2.44$ when $Re_d = 0.406$, $K \approx 3.42$ when $Re_d = 0.677$ and $K \approx 4.39$ when $Re_d = 0.948$. Figure 3(b) shows the theoretical prediction curve spanning the squeezing and dripping modes, with the experimental agreement deteriorating at Ca_c extremes. At $Ca_c < 0.2$, the rotor wall confinement and flow non-uniformity limit the droplet growth despite theoretical predictions of size increase from reduced external flow velocity, yielding the experimental diameters smaller than the theoretical values. Conversely, near the dripping-to-jetting transition boundary ($Ca_c > 0.7$), satellite droplets exceeding 25 % of the main droplet diameter reduce effective main droplet volume, causing experimental sizes to undershoot predictions, and the flow instability broadens the droplet size distribution. Despite these deviations, a strong agreement persists in central squeezing and dripping modes.

3.3. Quantitative analysis of jetting mode

The jetting mode is one of the most significant modes for the preparation microdroplets in open-space microfluidics (Zhu *et al.* 2023). Figure 4(a) illustrates a typical jet in RFF, highlighting the key parameters of the jet: jet diameter (d_j), droplet size (D_j), unstable wavelength (λ) and jet length (L_j). Variations in slit width significantly influence the downstream development of the jet. So d_j is defined as the width at the centre of the slit, while L_j extends from the conical end of the dispersed fluid to the jet breakup point, as shown in figure 4(a). Figures 4(b)–4(d) present the dimensionless droplet size, dimensionless jet length and dimensionless jet diameter for different flow control parameters, with the characteristic length being the inner diameter of the needle d_i. As Ca_c increases, both the jet diameter and droplet size decrease, while the jet length increases. Conversely, an increase in Re_d results in larger jet diameters, droplet sizes and jet lengths.

To quantify the experimental observations and analyse the global evolution of the dispersed phase within narrow slits, the continuous-phase flow field between the rotors is numerically simulated. The
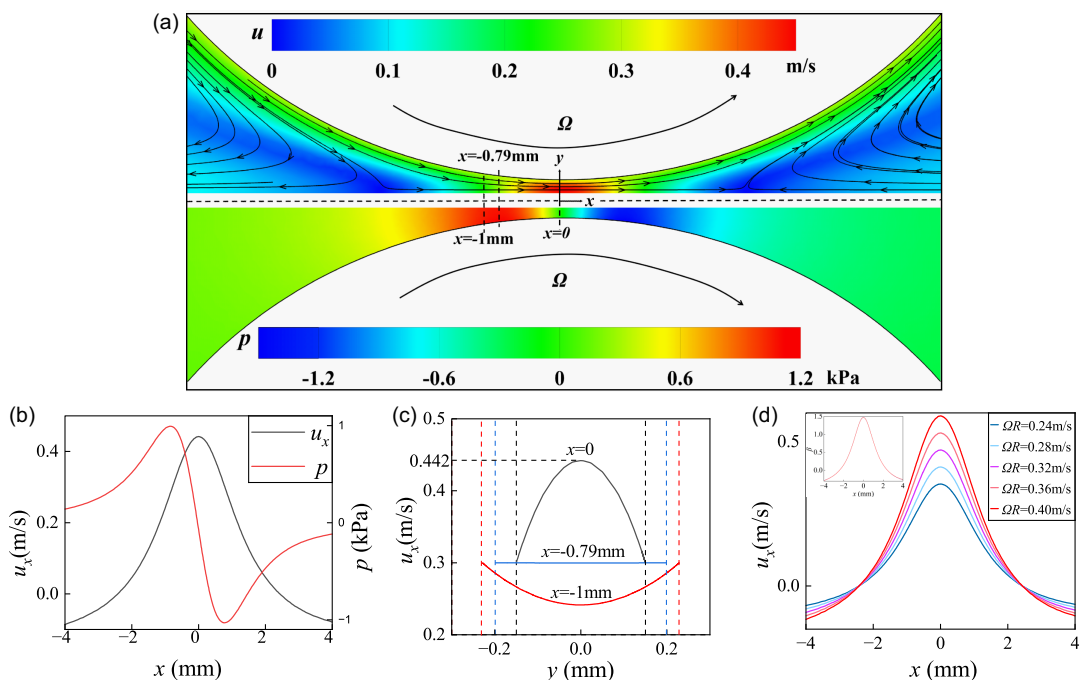
Figure 5. *Numerical simulation of the rotational shear flow field (rotational velocity $\Omega R = 0.3\,\mathrm{m\,s^{-1}}$ for a–c). (a) Velocity and pressure contour maps between narrow slits (origin at the centre of the slit throat). (b) Velocity distribution in the x direction (u_x) and pressure (p) along the x axis. (c) Velocity u_x across the channel cross-section at different x positions. (d) Velocity u_x along the x axis at varying rotational velocity.*

geometric parameters and fluid properties are set to match the experimental conditions, with the rotational velocity specified as $\Omega R = 0.3\,\mathrm{m\,s^{-1}}$ (detailed simulation methods are provided in Appendix A). Figure 5(a) displays the simulated velocity and pressure fields between two rotors (origin: the slit centre). The magnitude and direction of velocity contours and streamlines in the upper section are quantified. Flow contraction at the entrance accelerates the continuous fluid to maximum velocity at the throat, with a velocity decay downstream due to the flow expansion. Counter-flow vortices develop at both ends of the slit, opposing the primary flow. This flow topology aligns with prior double-rotor and four-rotor flow field studies (Dormy & Moffatt 2024; Jeffery 1922; Taylor 1934). The lower-section pressure distribution in figure 5(a) shows the entrance peak and the symmetric exit minimum. Figure 5(b) quantifies the continuous-phase influence via centreline axial velocity (u_x) and pressure (p) profiles, directly explaining the biconical jet morphology in figure 4(a). The mass conservation dictates jet necking at the throat forming characteristic waist-like profiles. Concurrently, the frontal pressure peaks drive post-needle dispersed-phase accumulation, generating the conical structures.

The velocity profiles at different positions within the slit are presented in figure 5(c), where they closely approximate parabolic shapes. To quantify the external flow field characteristics, the dimensionless velocity ratio $\beta = u_x/(\Omega R)$ is defined as the local x-direction velocity normalised by the rotational velocity. At $x = \pm 0.79\,\mathrm{mm}$, the x-direction velocity is nearly equal to the rotor wall velocity, yielding $\beta \approx 1$, whereas at the origin ($x = 0, y = 0$), β reaches a maximum of approximately 1.47. Figure 5(d) presents the x-velocity profiles and β-variation curves along the x-axial direction under varying rotational velocities. The results reveal that increasing the rotational velocity proportionally increases the velocity magnitude throughout the flow field; the overall structure of the velocity profile and the position of the stationary point remain unchanged.

After determining the basic structure of the external flow field, the interfacial evolution of the dispersed phase can be analysed. Within the experimental parameter range, it can be assumed that the flow velocity of the dispersed phase u_d is equal to that of the continuous phase u_c. According to the conservation of mass:

$$Q_d = u_d \frac{\pi d_j^2}{4} = \beta \Omega R \frac{\pi d_j^2}{4}, \tag{3.4}$$

and the dimensionless jet diameter can be related to Ca_c as follows:

$$d_j/d_i = \sqrt{\frac{4 Q_d \mu_c}{\pi \beta \gamma d_i^2}} Ca_c^{-1/2}. \tag{3.5}$$

Since the jet diameter is measured at the narrowest point of the slit, the value of β is 1.47. Figure 4(*b*) shows that the theoretical and experimental values of the jet diameter are in good agreement, which indirectly validates the numerical simulation.

As the jet develops downstream, it breaks up into a series of droplets due to capillary instability. The conservation of volume is satisfied during the jet breakup:

$$\lambda_{max} \frac{\pi d_j^2}{4} = \frac{4}{3} \pi D_j^3, \tag{3.6}$$

where λ_{max} is the most unstable wavelength. By substituting the most unstable wavelength of the jet $\lambda_{max} = \pi d_j / k_{max}$ and (3.5) into (3.6), the following can be obtained:

$$\frac{D_j}{d_i} = \frac{1}{d_i} \left(\frac{3}{2 k_{max} \sqrt{\pi}} \right)^{1/3} \left(\frac{\mu_c Q_d}{\gamma \beta} \right)^{1/2} Ca_c^{-1/2}. \tag{3.7}$$

In the analysis, two key dimensionless parameters are identified: the critical wavenumber k_{max} and the velocity ratio β. To facilitate the theoretical investigation of k_{max}, the model is simplified. Based on axisymmetric linear stability analysis (Si *et al.* 2009), it is found that the dimensionless critical wavenumber remains approximately constant at $k_{max} = 0.55$ under given experimental conditions (detailed calculations are provided in Appendix B). Regarding the velocity ratio β, it is observed that as the jet length increases, the value of β at the jet breakup point decreases from 1.17 to 0.42. Due to the rapid variation in the flow field near the jet breakup location, obtaining accurate β values under specific experimental conditions is challenging. Moreover, the upstream flow field also influences the droplet formation process. Therefore, in the theoretical formulation of (3.7), a representative value of $\beta = 1$ is adopted for all calculations. The corresponding theoretical predictions, indicated by the dashed lines in figure 4(*c*), exhibit good agreement with the experimental results.

It is important to note that variations in flow parameters also influence the jet length L_j, which follows the scaling law $L_j \sim u_d t_j$. The jet velocity u_d, as established earlier, is approximated by the continuous-phase velocity u_c in the jetting mode. The jet breakup time t_j is governed by the Ohnesorge number (Lister & Stone 1998), which is defined as $Oh_d = \mu_d / \sqrt{\rho_d d_j \gamma}$. Specifically, when $Oh \ll 1$, the breakup time is given by $t_j = \sqrt{\rho_d d_j^3 / \gamma}$, while for $Oh \sim 1$, it follows $t_j = \mu_d d_j / \gamma$. Under the experimental conditions, the Ohnesorge number of the dispersed phase is expressed as

$$Oh_d = \mu_d \left(\frac{\pi \beta \Omega R}{4 Q_d \rho_d^2 \gamma^2} \right)^{1/4} \sim O(0.1). \tag{3.8}$$

Accordingly, both time scales are considered separately, as presented in (3.9) and (3.10):

$$L_j \sim \left(\frac{4 Q_d}{\pi} \right)^{3/4} \left(\frac{\rho_d^2 \beta}{\mu_c \gamma} \right)^{1/4} Ca_c^{1/4}, \tag{3.9}$$

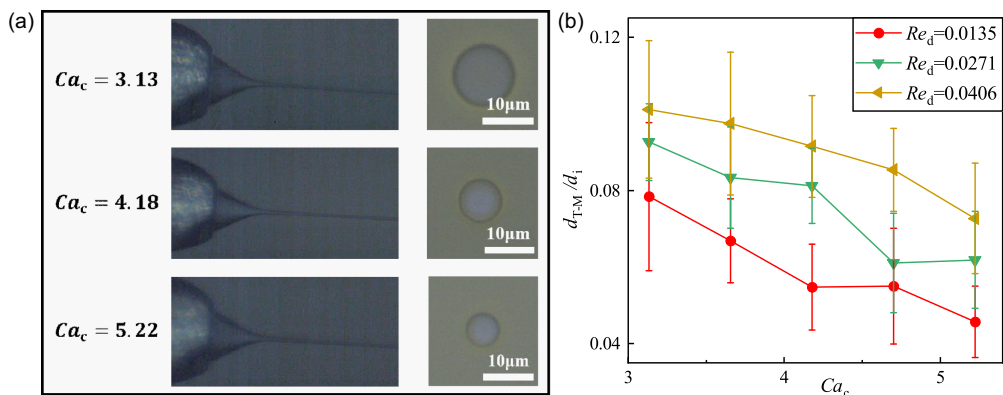$$L_j \sim \mu_d \sqrt{\frac{4 \beta Q_d}{\pi \gamma \mu_c}} Ca_c^{1/2}. \tag{3.10}$$

Figure 6. *Tip-streaming mode in RFF (geometric parameters: $L = 0$ mm and $d = 0.8$ mm). (a) Images of conical regions and droplets at different Ca_c ($Re_d = 0.0135$). (b) Dimensionless droplet diameter obtained from experiments as a function of Ca_c under varying Re_d.*

The actual jet length scale should lie between these two scaling laws. Figure 4(*d*) plots the two scaling curves. Experimental data indicate that when $L_j/d_i < 20$, the relative jet length follows the expected scaling law. However, as $L_j/d_i > 20$, the increase in relative jet length slows with rising Ca_c. This deviation is attributed to the fact that at $L_j/d_i = 20$, the velocity ratio $\beta = 1$ at the jet breakup point, while the axial velocity of the downstream continuous-phase flow rapidly decreases. In such a rapidly decelerating external flow field, the development of the dispersed-phase jet is hindered, leading to a departure from the theoretical scaling behaviour. Therefore, when employing the jetting mode for droplet generation, excessive rotational velocity and dispersed-phase flow rate should be avoided to ensure that $\beta > 1$ at the jet breakup position, thereby promoting the droplet formation in a relatively uniform flow field.

3.4. Experimental results on tip-streaming mode

In the tip-streaming mode, a conical fluid structure forms at the needle tip, where a slender jet emerges and subsequently breaks up into fine droplets. The droplet diameter can be one to two orders of magnitude smaller than the characteristic length scale of the device. However, the experimental observations indicate that stable tip-streaming becomes difficult to achieve when the rotor spacing d is small and the needle-to-rotor-connection-midpoint distance L is large. When geometric parameters are set to $d = 0.3$ mm and $L = 2$ mm, interfacial oscillations occur with intermittent tip-jet emergence, preventing uniform microdroplet formation. Conversely, adjusting parameters to $d = 0.8$ mm and $L = 0$ mm – effectively widening the slit and aligning the needle with the slit throat – establishes stable tip-streaming under identical flow conditions. Subsequent tip-streaming investigations maintain $d = 0.8$ mm and $L = 0$ mm, while § 3.5.1 details geometric parameter effects on interface evolution. As shown in figure 6(*a*), variations in Ca_c do not significantly alter the conical shape at the needle tip, although the droplet size changes substantially. To quantify the relationship between experimental parameters and droplet size, droplets are collected under a range of controlled conditions. The dimensionless droplet size as a function of Ca_c at different Re_d is presented in figure 6(*b*). The droplet diameter decreases monotonically with increasing Ca_c and decreasing Re_d. The droplet size is of the order of 10^{-5} m, while the production frequency can exceed the kilohertz range.

3.5. Discussion

3.5.1. Geometrical parameters

In the preceding analysis, the geometric parameters of the RFF device are not considered as a primary focus. However, as previously discussed, stable tip-streaming mode becomes difficult to achieve when
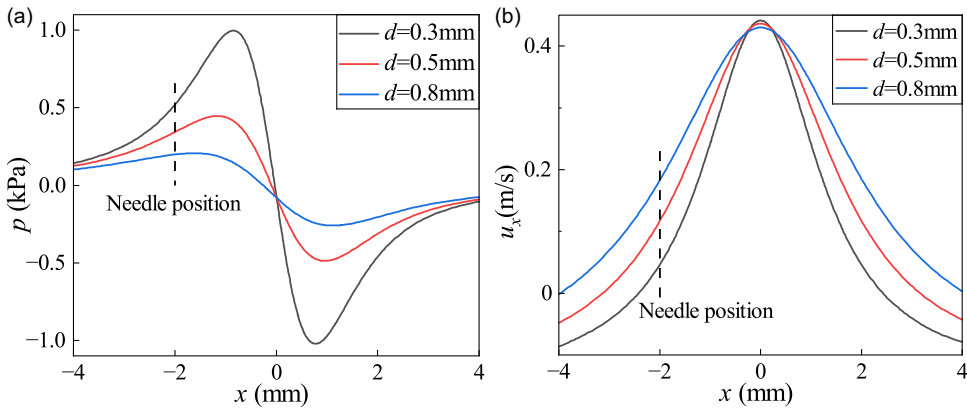
Figure 7. *(a) Pressure distribution along the x axis for different values of d. (b) Velocity distribution along the x axis in the x direction for different values of d.*

the rotor spacing d is small and the needle-to-rotor-connection-midpoint distance L is large, suggesting that geometric parameters play a critical role in the flow dynamics.

Figure 5(b) presents the pressure and velocity distributions along the x axis of the external flow field. A distinct pressure peak is observed near the front end of the slit, and its magnitude increases with higher rotational velocity. Under conditions of low dispersed-phase flow rate and high rotational velocity – characteristic of the tip-streaming mode – the dispersed phase accumulates and compresses upstream of the pressure peak, forming a conical interface. A fine jet is produced only after the tip of this cone crosses the pressure peak, resulting in the characteristic tip-streaming morphology. Once part of the accumulated fluid is ejected through the fine jet, the conical tip retracts upstream to the pressure peak, repeating the accumulation–jetting cycle. To establish a stable tip-streaming mode, L must be sufficiently small so that the needle tip resides downstream of the pressure peak. Reduced L also increases the velocity of the continuous phase at the needle tip, further promoting tip-streaming formation. Complementarily, figure 7 demonstrates how increased rotor spacing d reduces the pressure peak while accelerating and homogenising flow at the slit entrance – conditions favouring tip-streaming generation.

The influence of geometric parameters on other flow modes and their transition boundaries is also investigated. Figure 8(a,b) illustrates the effects of variations in L on the dripping and jetting modes, while figure 8(c) presents how changes in L affect the mode transition boundaries. Increased L reduces needle-tip velocity and enlarges the needle-to-pressure-peak distance. Consequently, droplet size expands in dripping mode, and the mode transition boundaries shift towards higher Ca_c (i.e. higher rotational velocity). Notably, the dripping to tip-streaming boundary for $L = 2.5\,\text{mm}$ is absent in figure 8(c) due to insufficient continuous-phase velocity for tip-streaming within tested parameters. In the jetting mode, L variations minimally affect jet breakup location and droplet diameter, as they solely alter the flow field at the needle outlet without affecting the downstream evolution process after jet formation. Figures 8(d) and 8(e) show the effects of varying rotor spacing on the dripping and jetting modes, respectively, and figure 8(f) illustrates the corresponding impact on the mode transition boundaries. Conversely, increased d reduces the pressure peak while boosting dispersed-phase flux at the needle tip. These alterations yield smaller droplets in the dripping mode and facilitate transitions to jetting and tip-streaming modes. Larger d also promotes uniform droplet formation in jetting mode by mitigating flow disturbances from rotor-shaft vibrations. Such vibrations – arising from inherent challenges in maintaining perfect concentricity between shaft and support – disrupt slit-proximal flow at high rotational velocity. Similarly, other geometric parameters are found to influence interfacial evolution. For instance, variations in rotor radius affect both the flow field structure and the pressure gradient within the slit, and an increased rotor radius promotes a more parallel flow field, facilitating stable droplet
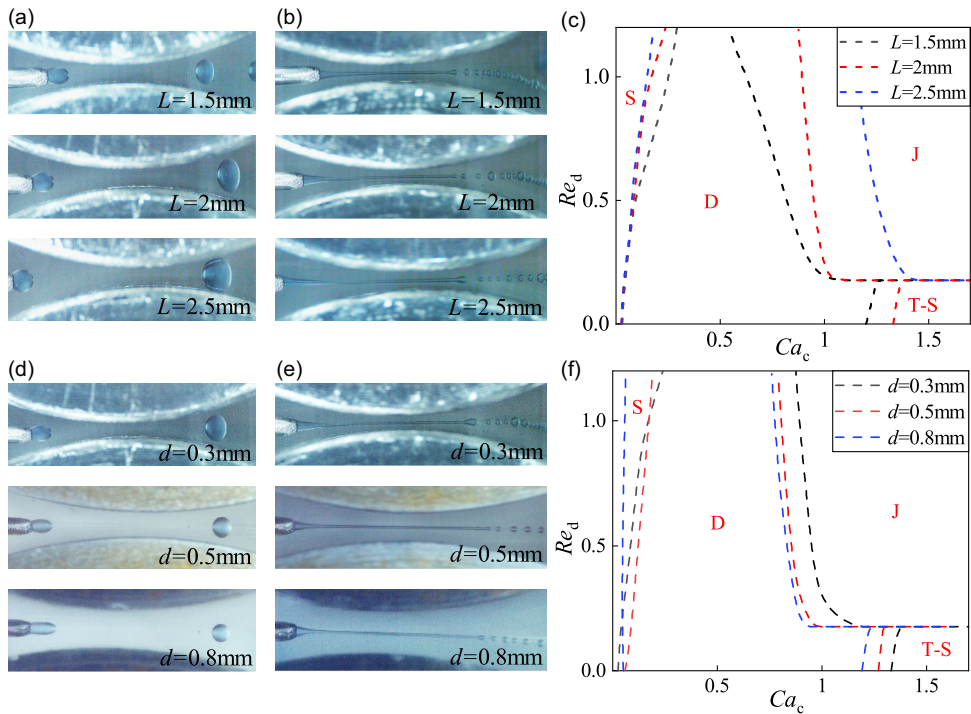
Figure 8. *(a) Influence of varying L on the dripping mode under constant flow parameters ($Re_d = 0.406$, $Ca_c = 0.362$). (b) Influence of varying L on the jetting mode under constant flow parameters ($Re_d = 0.677$, $Ca_c = 1.85$). (c) Influence of varying L on the boundary of mode transition. (d) Influence of varying d on the dripping mode under constant flow parameters ($Re_d = 0.406$, $Ca_c = 0.362$). (e) Influence of varying d on the jetting mode under constant flow parameters ($Re_d = 0.677$, $Ca_c = 1.85$). (f) Influence of varying d on the boundary of mode transition.*

generation. Moreover, an increase in rotor height helps to suppress vertical three-dimensional effects, further contributing to the stability of interfacial evolution. These findings collectively indicate that, within an appropriate range, increasing d and R while decreasing L promotes the stable production of uniform microdroplets.

3.5.2. Physical properties

In RFF, the physical properties of fluids also significantly influence microdroplet formation. For instance, the interfacial shear stress between fluids is defined as $\tau = \mu(du/dy)$, where μ denotes the dynamic viscosity of the continuous phase and du/dy represents the velocity gradient. A higher viscosity of the continuous phase results in a larger interfacial shear force, thereby promoting the breakup of the dispersed phase and facilitating microdroplet generation. To investigate the influence of fluid viscosity on droplet formation, a series of experiments are conducted using glycerol aqueous solution (140−900 mPa s) as the continuous phase and silicone oils (9.15−1043 mPa s) as the dispersed phase.

The results demonstrate that an increase in the viscosity ratio N advances the transition from dripping to jetting mode. Furthermore, elevated viscosity in either phase facilitates dripping-to-jetting and dripping-to-tip-streaming mode transitions at lower rotational velocity, thereby demonstrating the distinct advantage of RFF for high-viscosity fluid processing. Regarding droplet size, when using high-viscosity fluids – specifically glycerol (900 mPa s) as the continuous phase and silicone oil (1043 mPa s) as the dispersed phase – droplets ranging from $8.77 \pm 2.38\,\mu m$ ($Re_d = 0.0135$, $Ca_c = 6.267$) to $1.71 \pm 0.06\,mm$ ($Re_d = 0.948$, $Ca_c = 0.0084$) are produced under the same geometric

conditions ($L = 0\,\mathrm{mm}$, $d = 0.8\,\mathrm{mm}$). These results confirm that the RFF system is capable of generating droplets across a wide size spectrum, from the micrometre to millimetre scale, and further demonstrate its potential for processing high-viscosity fluids in droplet-based applications. Additionally, under extreme conditions where the dispersed phase is air, steep pressure gradients in the continuous-phase flow field coupled with air's high compressibility cause fragmentation into bubbles at the needle tip – precluding stable structure formation under current experimental configurations.

4. Conclusions

The RFF technique is systematically investigated in this study through the integration of experimental observations and numerical simulations, whereby the primary flow modes – squeezing, dripping, jetting and tip-streaming – are identified. The transitions between these modes are delineated by varying the key dimensionless parameters, namely the Reynolds number of the dispersed phase (Re_d) and the capillary number of the continuous phase (Ca_c). For each mode, the relationships between the flow control parameters and characteristic quantities are quantitatively examined. In the squeezing and dripping modes, droplet size correlations under varying Re_d and Ca_c are derived based on kinetic analysis during detachment. In the jetting mode, numerical simulations of the external flow field are conducted to analyse the flow structure of the RFF. Scaling laws for jet diameter, droplet size and jet length are established, demonstrating consistency with experimental results. In the tip-streaming mode, the influence of flow parameters on droplet size is quantitatively characterised, confirming that the RFF technique can reliably generate micrometre-scale droplets. In addition to flow parameters, the influence of geometric parameters is evaluated. Experimental results indicate that a larger rotor spacing (d) and a shorter needle-to-rotor-connection-midpoint distance (L) enhance the stability and uniformity of microdroplet formation. The influence of viscosity in both dispersed and continuous phases on interfacial evolution is investigated. Additionally, high-viscosity microdroplets ranging from the micrometre to millimetre scale are successfully produced. This comprehensive study provides theoretical insights into the effects of flow and geometric parameters on interfacial evolution and droplet formation in RFF systems, offering valuable guidance for the efficient fabrication of high-viscosity microdroplets in future applications.

References

Cubaud, T., & Mason, T. G. (2008). Capillary threads and viscous droplets in square microchannels. *Physics of Fluids*, *20*(5), 053302.

Dormy, E., & Moffatt, H. K. (2024). Flow induced by the rotation of two circular cylinders in a viscous fluid. *Physical Review Fluids*, *9*(4), 044102.

Garstecki, P., Stone, H. A., & Whitesides, G. M. (2005). Mechanism for flow-rate controlled breakup in confined aeometries: A route to monodisperse emulsions. *Physical Review Letters*, *94*(16), 164501.

Gañán-Calvo, A. M. (1998). Generation of steady liquid microthreads and micron-sized monodisperse sprays in gas streams. *Physical Review Letters*, *80*(2), 285–288.

Gañán-Calvo, A. M. (2007). Electro-flow focusing: The high-conductivity low-viscosity limit. *Physical Review Letters*, *98*(13), 134503.

Gañán-Calvo, A. M., & Barrero, A. (1999). A novel pneumatic technique to generate steady capillary microjets. *Journal of Aerosol Science*, *30*(1), 117–125.

Gañán-Calvo, A. M., & Montanero, J. M. (2009). Revision of capillary cone-jet physics: Electrospray and flow focusing. *Physical Review E*, *79*(6), 066305.

Guerrero, J., Chang, Y. W., Fragkopoulos, A. A., & Fernandez-Nieves, A. (2020). Capillary-based microfluidics-coflow, flow-focusing, electro-coflow, drops, jets, and instabilities. *Small*, *16*(9), 1904344.

He, L. Y., Wang, B., Liu, Q. Q., & Chan, X. D. (2025). Interface evolution of microdroplets in flow-focusing channels with varying aspect ratios. *Flow*, *5*, E19.

Herrada, M. A., Gañán-Calvo, A. M., Ojeda-Monge, A., Bluth, B., Riesco-Chueca, P. (2008). Liquid flow focused by a gas: Jetting, dripping, and recirculation. *Physical Review E*, *78*(3), 036323.

Hert, S. C. D., & Rodgers, T. L. (2018). On the steady-state drop size distribution in stirred vessels. Part I: Effect of dispersed phase viscosity. *Aiche Journal*, *64*(9), 3293–3302.

Hohman, J. N., Kim, M., Wadsworth, G. A., Bednar, H. R., Jiang, J., LeThai, M. A., Weiss, P. S. (2011). Directing substrate morphology via self-assembly: Ligand-mediated scission of gallium-indium microspheres to the nanoscale. *Nano Letters*, *11*(12), 5104–5110.

Jeffery, G. B. (1922). The rotation of two circular cylinders in a viscous fluid. *Proceedings of the Royal Society of London. Series A, Containing Papers of a Mathematical and Physical Character*, *101*(709), 169–174.

Li, K., Gong, K., Liu, J., Ohnoutek, L., Ao, J., Liu, Y., Chen, X., Xu, G., Ruan, X., Cheng, H., Han, J., Sui, G., Ji, M., Valev, V. K., Zhang, L. (2022). Significantly accelerated photochemical and photocatalytic reactions in microdroplets. *Cell Reports Physical Science*, *3*(6), 100917.

Li, X., Li, M., Zong, L., Wu, X., You, J., Du, P., Li, C. (2018). Liquid metal droplets wrapped with polysaccharide microgel as biocompatible aqueous ink for flexible conductive devices. *Advanced Functional Materials*, *28*(39), 1804197.

Liang, F., Kahouadji, L., Valdes, J. P., Shin, S., Chergui, J., Juric, D., Matar, O. K. (2022). Numerical study of oil–water emulsion formation in stirred vessels: Effect of impeller speed. *Flow*, *2*, E34.

Lister, J. R., & Stone, H. A. (1998). Capillary breakup of a viscous thread surrounded by another viscous fluid. *Physics of Fluids*, *10*(11), 2758–2764.

Markvicka, E. J., Bartlett, M. D., Huang, X., Majidi, C. (2018). An autonomously electrically self-healing liquid metal–elastomer composite for robust soft-matter robotics and electronics. *Nature Materials*, *17*(7), 618–624.

Marín, A. G., Campo-Cortés, F., & Gordillo, G. M. (2009). Generation of micron-sized drops and bubbles through viscous coflows. *Colloids and Surfaces A: Physicochemical and Engineering Aspects*, *344*(1), 2–7.

Mu, K., Si, T., & Ding, H. (2019). Nonlinear dynamics and manipulation of dripping in capillary flow focusing. *Physical Review E*, *78*(3), 036323.

Rosell-Llompart, J., & Gañán-Calvo, A. M. (2008). Turbulence in pneumatic flow focusing and flow blurring regimes. *Physical Review E*, *77*(3), 036321.

Saffarionpour, S. (2019). Preparation of food flavor nanoemulsions by high- and low-energy emulsification approaches. *Food Engineering Reviews*, *11*(4), 259–289.

Sheth, T., Seshadri, S., Prileszky, Tás, Helgeson, M. E. (2020). Multiple nanoemulsions. *Nature Reviews Materials*, *5*(3), 214–228.

Si, T. (2021). Dynamic behavior of droplet formation in dripping mode of capillary flow focusing. *Capillarity*, *4*(3), 45–49.

Si, T., Li, F., Yin, Y. X., & Yin, X. Z. (2009). Modes in flow focusing and instability of coaxial liquid–gas jets. *Journal of Fluid Mechanics*, *629*, 1–23.

Si, T., Li, F., Yin, Y. X., & Yin, X. Z. (2010). Spatial instability of coflowing liquid-gas jets in capillary flow focusing. *Physics of Fluids*, *22*(11), 112105.

Taylor, G. I. (1934). The formation of emulsions in definable fields of flow. *Proceedings of the Royal Society of London. Series A, Containing Papers of a Mathematical and Physical Character*, *146*(858), 501–523.

Umbanhowar, P. B., Prasad, V., & Weitz, D. A. (1999). Monodisperse emulsion generation via drop break off in a coflowing stream. *Langmuir*, *16*(2), 347–351.

Utada, A. S., Fernandez-Nieves, A., Stone, H. A., & Weitz, D. A. (2007). Dripping to jetting transitions in coflowing liquid streams. *Physical Review Letters*, *99*(9), 094502.

Utada, A. S., Lorenceau, E., Link, D. R., Kaplan, P. D., Stone, H. A., Weitz, D. A. (2005). Monodisperse double emulsions generated from a microcapillary device. *Science*, *308*(5721), 537–541.

Vega, E. J., Montanero, J. M., Herrada, M. A., & Gañán-Calvo, A. M. (2010). Global and local instability in flow focusing: The influence of the geometry. *Physics of Fluids*, *22*(6), 064105.

Wang, S., Zhu, Z., Ma, C., Qiao, R., Yang, C., Xu, R. X., Si, T. (2021). Generation of nonspherical liquid metal microparticles with tunable shapes exhibiting an electrostatic-responsive performance. *ACS Applied Materials Interfaces*, *13*(14), 16677–16687.

Xu, Z., Wang, S., Zhao, C., Li, S., Liu, X., Wang, L., Li, M., Huang, X., Mann, S. (2020). Photosynthetic hydrogen production by droplet-based microbial micro-reactors under aerobic conditions. *Nature Communications*, *11*(1), 5985.

Yun, G., Tang, S.-Y., Sun, S., Yuan, D., Zhao, Q., Deng, L., Yan, S., Du, H., Dickey, M. D., Li, W. (2019). Liquid metal-filled magnetorheological elastomer with positive piezoconductivity. *Nature Communications*, *10*(1), 1300.

Zhu, Z., Chen, T., Huang, F., Wang, S., Zhu, P., Xu, R. X., Si, T. (2023). Free-boundary microfluidic platform for advanced materials manufacturing and applications. *Advanced Materials*, *36*(7), 2304840.

Zhu, P. A., & Wang, L. Q. (2017). Passive and active droplet generation with microfluidics: A review. *Lab on a Chip*, *17*(1), 34–75.